

Dual-view transport of intensity phase imaging flow cytometry

AIHUI SUN,^{1,†}  YAXI LI,^{2,†} PENGFEI ZHU,¹ XIAOLIANG HE,¹
ZHILONG JIANG,¹  YAN KONG,^{1,3}  CHENG LIU,^{1,3} AND SHOUYU
WANG^{4,5,*} 

¹Department of Optoelectronic Information Science and Engineering, School of Science, Jiangnan University, Wuxi, Jiangsu, 214122, China

²Radiology Department, Jiangnan University Medical Center, Wuxi, Jiangsu, 214122, China

³Shanghai Institute of Optics and Fine Mechanics, Chinese Academy of Sciences, Shanghai, 201800, China

⁴Jiangsu Province Engineering Research Center of Integrated Circuit Reliability Technology and Testing System & School of Electronics and Information Engineering, OptiX+ Laboratory, Wuxi University, Wuxi, Jiangsu 214105, China

⁵Single Molecule Nanometry Laboratory, China

[†]These authors contributed equally to this work.

*shouyu29@cwxiu.edu.cn

Abstract: In this work, we design multi-parameter phase imaging flow cytometry based on dual-view transport of intensity (MPFC), which integrates phase imaging and microfluidics to a microscope, to obtain single-shot quantitative phase imaging on cells flowing in the microfluidic channel. The MPFC system has been proven with simple configuration, accurate phase retrieval, high imaging contrast, and real-time imaging and has been successfully employed not only in imaging, recognizing, and analyzing the flowing cells even with high-flowing velocities but also in tracking cell motilities, including rotation and binary rotation. Current results suggest that our proposed MPFC provides an effective tool for imaging and analyzing cells in microfluidics and can be potentially used in both fundamental and clinical studies.

© 2023 Optica Publishing Group under the terms of the [Optica Open Access Publishing Agreement](#)

1. Introduction

As a widely used technique in biological and medical fields, flow cytometry employs scattered light or fluorescence to detect the physical and chemical characteristics of cells [1,2]. In detail, the forward-scattered light is used to measure the cellular sizes, the side-scattered light is used to indicate the granularity or internal complexity of the cells, and the fluorescence signal is used to detect the molecules such as proteins or nucleic acids in the cells. Often relying on high-performance single-pixel photodetectors such as photomultiplier tubes, conventional flow cytometry can sensitively and rapidly detect cellular characteristics. However, the measured signals only reflect the general characteristics while losing the particulars. For example, flow cytometry can measure cellular sizes but cannot provide their morphology. It is because the single-pixel photodetector only collects the light signal integrals while losing their corresponding spatial positions. Though conventional flow cytometry accelerates the detection speed, it inevitably reduces the sensing specificity and accuracy.

To solve this problem, imaging flow cytometry is a promising approach [3–5]. Galvo scanning systems have been widely used to detect every point of a flowing cell in microfluidics [6–8]. Besides, the spatial-temporal transformation was reported by inserting a known mask into conventional flow cytometry to simplify the system, and the function of the mask is to implement spatial sampling equivalent to the Galvo scanning system [9]. These methods obtain 2-D images via spatial point scanning, inevitably reducing the imaging speed. To accelerate the scanning speed, one breakthrough is serial time-encoded amplified microscopy [10,11]. Its key idea is

to first use the grating-generated space-encoded spectral signals for 2-D detection and then collect these spectral signals, which are further time-encoded by the dispersion fiber, using the single-pixel photodetector. In other words, each point of the cell can be detected by light at a specific wavelength, which is collected by the single-pixel photodetector at a specific sequence. Similarly, other optofluidic time-stretch imaging techniques have been designed [12]. For example, fluorescence radiofrequency-tagged emission can support imaging flow cytometry but is based on radiofrequency for signal encoding [13,14]. In addition, free-space angular-chirp-enhanced delay (FACED) combining laser scanning for spatial scanning and a FACED mirror pair for time stretching can be used at an ultrafast speed [15,16]. These above-mentioned imaging flow cytometers are all based on single-pixel photodetectors, which are beneficial for rapid and sensitive detection.

However, these imaging flow cytometers are often bulky and complicated due to the many inserted optical elements and devices. With the rapid development of image array sensors with higher frame rates and signal-to-noise ratios, imaging flow cytometry can be simplified by integrating the single-cell imaging capability of microscopy with the high-throughput capability of conventional flow cytometry. Imaging flow cytometry has been applied in different imaging modalities. As with microscopy, fluorescence imaging flow cytometry can specifically detect cells in the highest contrast but needs labeling during cell pretreatment [17,18]. Bright-field imaging flow cytometry has the simplest scheme but suffers from low contrast, especially in label-free conditions [19–21]. Different from those fluorescence and bright-field imaging ones, quantitative phase imaging flow cytometry can measure cellular morphology in high contrast, especially in label-free cases. Therefore, quantitative phase imaging-based flow cytometry has drawn a lot of attention due to its high performance in cellular detection applications.

Various quantitative phase imaging flow cytometers have been designed, and many of them are based on holography and interferometry [22–24]. It is because the quantitative phase can be reconstructed from a single-shot hologram or interferogram. However, many of these interference-based quantitative phase imaging flow cytometers have complicated systems with separated sample and reference arms. Though in-line holography and common-path interferometry can partially solve the problem [25,26], these interference-based quantitative phase imaging techniques suffer from a time-consuming phase retrieval process, especially phase unwrapping. Besides holography and interferometry, a coherent modulated imaging flow cytometer has been recently reported with an extremely simple optical scheme [27]. But still, it takes a long time for iterative phase retrieval.

Though the transport of intensity phase imaging requires multi-focal images for phase reconstruction, many techniques have been reported to obtain these multi-focal images in a single shot, such as based on dispersion [28], beam splitting [29,30], diffraction [31–33], and so on. Among them, our previously designed dual-view transport of intensity phase imaging can obtain single-shot phase distribution from simultaneously captured under- and over-focus images with the advantages of simple configuration and a large field of view (FoV) [34,35]. It has been successfully used in live cell observation [36] and whole-slide imaging [37,38]. Besides, the transport of intensity phase imaging can reconstruct phase at a fast speed without phase unwrapping or iterative phase retrieval. Therefore, it is also a promising tool for quantitative phase imaging flow cytometry. In this work, we designed dual-view transport of intensity phase imaging flow cytometry, which combines phase microscopy and microfluidics. Since MPFC can provide cellular multi-parameters such as amount, phase, and morphology (area, eccentricity, diameter, and so on), it can be employed not only in imaging and analyzing flowing cells but also in tracking cell motility. We believe that this work expands the application scope of the dual-view transport of intensity phase imaging and is expected to promote the application of phase imaging flow cytometry in high-throughput rapid cellular detection.

2. Experimental setup

Figure 1(a) shows the proposed MPFC system, which is based on a commercial Nikon microscope (Eclipse Ti2-E, Japan) equipped with a board-level camera integrated with two CMOS imaging chips (1280×1024 , $4.8 \mu\text{m}$, Daheng Imaging, China). In detail, the beam emitted from a LED passes through an interference filter (central wavelength = 532 nm , FWHM = 10 nm , Daheng Optics, China) and serves as the light source for Kohler illumination. The microfluidic channel with the length, width, and depth of 20 mm , $200 \mu\text{m}$, and $200 \mu\text{m}$, as shown in the yellow box, is fixed on the microscope sample stage. Using a micromolecular injection pump (LSP Rongbai, China), the cell solution can be injected into the microfluidic channel and driven finally into the recycling dish. A micro-objective ($10\times$, N.A. = 0.25) is employed to image these cells. After the tube lens, a board-level camera is used for simultaneous under- and over-focus image recording for phase retrieval. In brief, a prism (Daheng Optics, China) is used to spilt the wavefront output from the microscope: one is collected with a CMOS camera located before the imaging plane with a defocus distance of 1 mm , and another is collected with another CMOS camera (Daheng Imaging, China) located after the imaging plane with a defocus distance of 1 mm . It should be noted that the FoVs of simultaneously captured under- and over-focus images have been corrected in advance based on the phase correlation approach to guarantee accurate phase retrieval. Moreover, the in-focus image is approximated by the average of the FoV-corrected under- and over-focus images. Therefore, according to the computed in-focus image, focus adjustment in the MPFC system is almost the same as that in a conventional microscope.

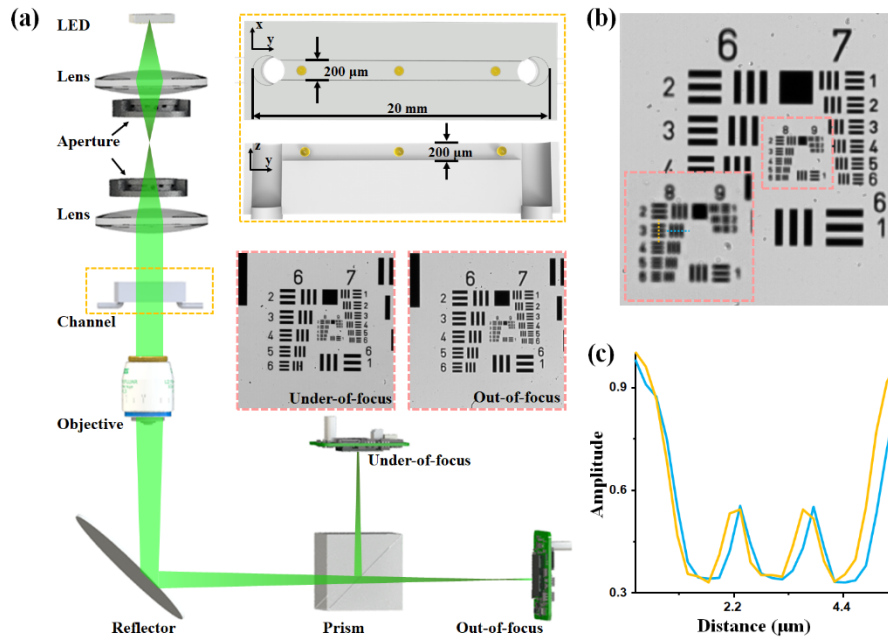


Fig. 1. (a) Scheme of MPFC system: the yellow inset is a zoomed-in view of the microfluidic chip, and the pink inset shows the images acquired by the two CMOS. (b) Computed in-focus image of a USAF 1951 resolution test chart. (c) Cross-sections of the line pairs of Group 8 Element 3.

The quantitative phase can be reconstructed by solving the Poisson equation in Eq. (1), in which k is the wave number, ∇ is the gradient operator, $I(x, y)$ and $\frac{\partial I(x, y)}{\partial z}$ represent the in-focus

image and the image derivative, respectively, and $\varphi(x, y)$ is the phase under reconstruction.

$$k \frac{\partial I(x, y)}{\partial z} = -\nabla \cdot [I(x, y) \nabla \varphi(x, y)] \quad (1)$$

According to the principle of dual-view transport of intensity phase imaging, the in-focus can be obtained as the average of under- and over-focus images described in Eq. (2), and the image derivative is computed according to Eq. (3). In these two equations, $I(x, y, -\Delta z)$ and $I(x, y, \Delta z)$ respectively represent the under- and over-focus images, and Δz is the defocus distance.

$$I(x, y) = \frac{I(x, y, -\Delta z) + I(x, y, \Delta z)}{2} \quad (2)$$

$$\frac{\partial I(x, y)}{\partial z} = \frac{I(x, y, -\Delta z) - I(x, y, \Delta z)}{2\Delta z} \quad (3)$$

By substituting Eqs. (2) and (3) into Eq. (1), phase under detection can be reconstructed using the classical fast Fourier transform-based differential equation solver, which can be found anywhere [37,38].

Before application, the MPFC system was calibrated and verified. First tested by a USAF 1951 resolution test chart (Edmund Optics, US) in Fig. 1(b), the FoV of the MPFC system could reach 0.16 mm^2 , and the lateral resolution of the system was $1.55 \mu\text{m}$ since Group 8 Element 3 can be distinguished in Fig. 1(c). Additionally, a single pixel size represents $0.21 \mu\text{m}$. The calibrated FoV and lateral resolution of the MPFC system fully satisfied cellular imaging within the microfluidic channel.

Afterward, using a two-step random phase plate with a fabricated phase distribution difference of π at 532 nm , the phase retrieval accuracy of the MPFC system was tested. Figures 2(a1) and (a2) reveal the FoV-corrected under- and over-focus images, and Fig. 2(c) shows the computed in-focus one, proving that MPFC system can provide simultaneously captured multi-focus images in high quality. Via solving the Poisson equation, the phase was retrieved in Fig. 2(c), and the cross-sectional phase distribution in Fig. 2(d1) fitted well with the fabricated one, proving the high-accurate phase retrieval of the MPFC system.

Finally, the dynamic phase imaging performance of the MPFC system was verified using flowing cells in the microfluidic channel. After centrifugation, C6 cells were added to 0.5 mL paraformaldehyde solution and then mixed with PBS solution to prepare the cell solution. The C6 cell solution at a concentration of $1 \times 10^5 \text{ cells/mL}$ was injected into a microfluidic channel with a flow rate of $3.6 \mu\text{L/min}$. The frame rate of the CMOS camera was fixed as 33 fps, and the exposure time was set to $10 \mu\text{s}$. Figures 2(e1) and (e2) present the under- and over-focus images acquired simultaneously by the MPFC system, and Fig. 2(f) exhibits the computed in-focus one. Since the cells were almost transparent, only their outlines could be faintly observed in the bright-field modality. Figure 2(g) shows the cellular phase image with a significantly enhanced contrast compared to those in Figs. 2(e1) and 2(e2), and the cellular contour can be extracted from the retrieved phase, such as in Fig. 2(d2). It should be noted that there were also no significant motion blurs in both bright-field and phase imaging modalities, proving that the MPFC system worked well in imaging dynamic samples. According to the results in Fig. 2, it is proven that our proposed system can deal with phase imaging flow cytometry of high quality.

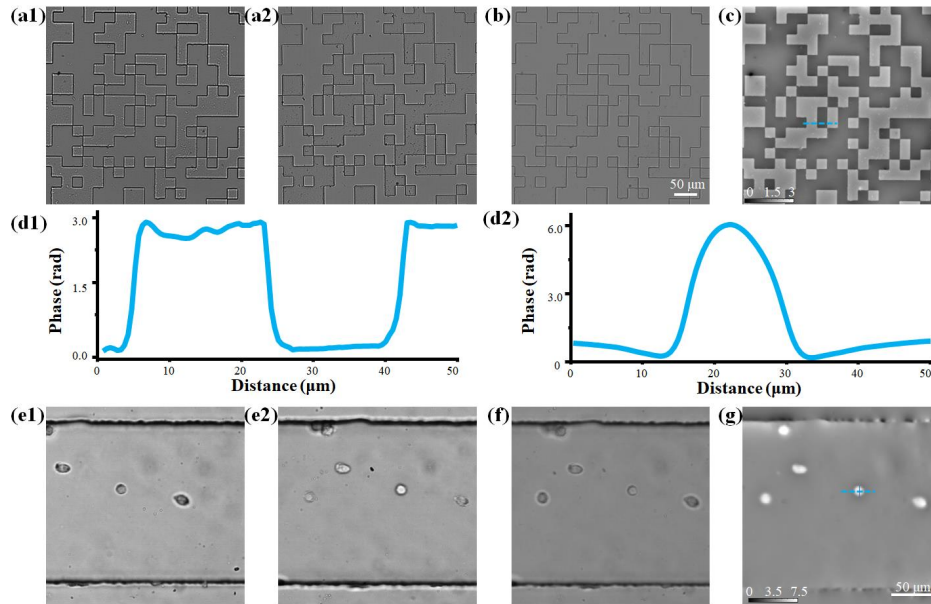


Fig. 2. (a) FoV-corrected under- and over-focus images of random phase plate; (b) Computed in-focus images; (c) Retrieved phase images of random phase plate; (d1) Cross-sectional phase images of random phase plate; (e) FoV-corrected under- and over-focus images of flowing cells in the microfluidic channel; (f) Computed in-focus images; (g) Retrieved phase images of cells; (d2) Cross-sectional phase images of cells; The white bars in (b), (g) and (g) indicate 50 μm , and the color bars in (c) and (g) represent phase values.

3. Result

First, the classical functions of cell imaging, recognition, and analysis of the MPFC system were tested. The C6 cell solution with a concentration of 1×10^5 cells/mL was injected into the microfluidic chip at a moderate flow rate of 3.6 $\mu\text{L}/\text{min}$. The exposure time of the CMOS cameras was set to 6 μs . Using the MPFC system, a 12-second movie ([Visualization 1](#)) reveals the reconstructed phases of a fixed FoV with cells flowing in the microfluidic channel. In [Visualization 1](#), the upper left value represents recording time, and the upper right value represents the time consumed in phase retrieval and data saving. Since the image processing time was around 25 ms and the frame rate of the CMOS camera was 33 fps, the MPFC system could satisfy the demand for real-time imaging. Figure 3(a) lists some of them at different moments, which provide significant contrast between cells and background. Therefore, cells could be precisely recognized using the threshold segmentation revealed in Fig. 3(b). According to the recognition results, cellular multi-parameters, such as diameter, area, eccentricity, and phase, can be extracted by combining the phase map with the binarized image. In detail, the cellular diameter was estimated using the number of pixel points. To quantitatively evaluate the cellular roundness, we also computed the eccentricity using $(d_{\text{max}} - d_{\text{min}})/(d_{\text{max}} + d_{\text{min}})$, where d_{max} and d_{min} are the long and short axes of the cells, respectively. As shown in Fig. 3(c), the eccentricities of most cells were less than 0.25, showing that cells were close to spherical shapes. Since a single pixel represents $0.21 \times 0.21 \mu\text{m}^2$ previously calibrated using the USAF 1951 resolution test chart, the cellular area was computed by the multiplication of a single-pixel-represented area and cell-occupied pixels. According to the results in Fig. 3(d), most C6 cells had areas between 240 μm^2 and 260 μm^2 . With the phase imaging modal, we also presented the phase statistics of the

cells in Fig. 3(d) by calculating the average phase value of individual cells, demonstrating that the cellular phase shows a positive correlation with the cellular area. It is proven that the MPFC system could provide cellular multi-parameters such as amount, phase, and morphology, thus satisfying the demands of the imaging flowing cytometry.

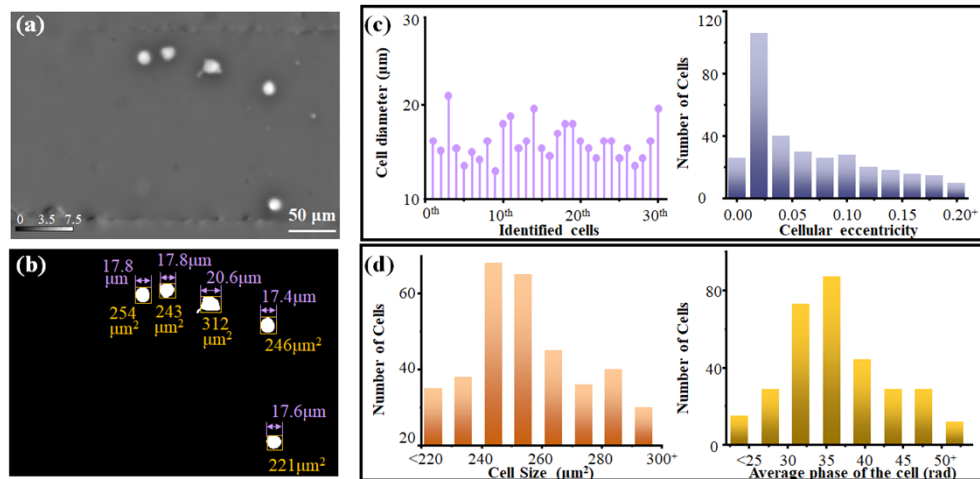


Fig. 3. Cell imaging, recognition, and analysis using the MPFC system in moderate-flowing velocity conditions. (a) Cell phase images (see [Visualization 1](#)); (b) Cell recognition; (c) Cellular diameter and eccentricity analysis; (d) Cellular area and phase analysis. The white bar in (a) indicates 50 μm, and the color bars in (a) represent phase values.

To further evaluate the performance of the MPFC system in high-flowing velocity conditions, we increased the flow rate to 31 μL/min, and the linear velocity of the cell in this channel was 13 mm/s. Here, the exposure time of the CMOS cameras was set to 1 μs to reduce motion artifacts. A 8-second movie ([Visualization 2](#)) reveals the reconstructed phases of a fixed FoV with cells flowing in the microfluidic channel. Figure 4(a) lists some of them at different moments, and there were few motion artifacts in these reconstructed phase images. Therefore, according to the threshold segmentation, the MPFC system can accurately recognize the number of cells in Fig. 4(b). Moreover, considering the flow rate, cell concentration, and microfluidic channel size, around 50 C6 cells flowed through the imaging FoV per second in theory. Figure 4(c) exhibits the counting results per second using the MPFC system, and Fig. 4(d) lists the cell counting of each frame within a second, demonstrating that around 40-60 cells flowed through the imaging FoV in a second, in agreement with the theoretical value. Due to the motion artifact-free reconstructed phase images in Fig. 4(a) and the accurate cell counting in Figs. 4(c) and 4(d), it is proven that the MPFC system performed well even in high-flowing velocity conditions.

Besides the conventional functions of imaging flow cytometry, the proposed MPFC system can also be employed to track cell motility in the microfluidic channel. It is because the MPFC system had high frame rates in phase imaging, thus providing a tool for imaging transient events. In this study, the flow rate of the cell solution was set to 3.6 μL/min, the linear velocity of the cells was calculated as 1.5 mm/s, and the exposure time of the MPFC system was set to 10 μs. Figure 5 shows several cell motilities, including rotation and binary rotation.

Figure 5(a) shows an example of a cell rotation in the x-y plane. Since the cell was not round, the rotation in the x-y plane can be easily distinguished according to the marked arrows in the zoomed-in subplots in the reconstructed phases at different moments in Fig. 5(a1). To further investigate the rotation plane, we checked the phase contours at different moments, as revealed in Fig. 5(a2). The phase did not change much during the cell flowing through the microfluidic

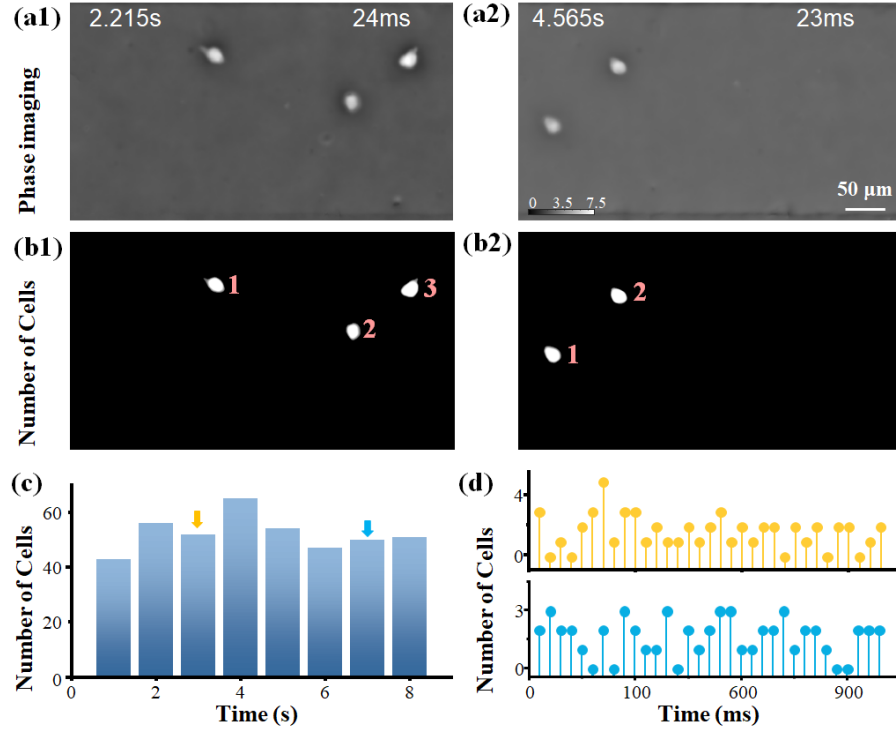


Fig. 4. Cell imaging, recognition, and analysis using the MPFC system in high-flowing velocity conditions. (a) Cell phase images (see Visualization 2); (b) Cell recognition; (c) Cell counting; (d) Cell counting of each frame with a second. The white bar in (a2) indicates 50 μm , and the color bars in (a2) represent phase values.

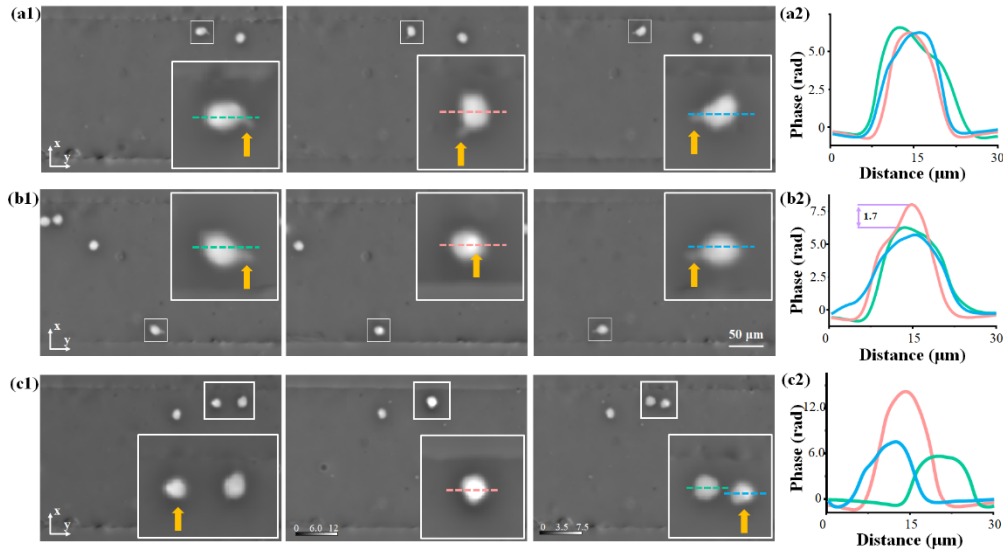


Fig. 5. Cell motility tracking using the MPFC system. (a) Cell rotation in the x-y plane; (b) Cell rotation in the y-z plane; (c) Binary cell rotation in the y-z plane. (1) Reconstructed phase and zoomed-in FoV at different moments; (2) Phase contours along the dotted lines in (1). The white bar in (c3) indicates 50 μm , and the color bars in (a) represent phase values.

channel, indicating that the cell rotated in the x-y plane. Figure 5(b) shows another example of a cell rotation but in the y-z plane. According to the reconstructed phase distributions as well as the zoomed-in subplots in Fig. 5(b1), the cell was determined to rotate in the y-z plane. To prove it, the phase contours at different moments are displayed in Fig. 5(b2), which shows significant phase changes during cell motility. These results in Fig. 5(b) verify that the cell rotated in the x-y plane.

Figure 5(c) shows a more interesting binary rotation example. According to the reconstructed phase distributions at different moments in Fig. 5(c1), two cells co-rotated in the y-z plane since their relative positions exchanged when they were flowing through the microfluidic channel. Compared to Fig. 5(c1), the phase contours in Fig. 5(c2) explain the binary rotation motility more clearly: when two cells overlapped, the measured phase is the phase sum of the individual cells, fully proving the motion of binary cells.

4. Conclusion

In this work, we proposed the MPFC system, which provides an excellent phase imaging flow cytometry platform for the study of cells in microfluidics. Based on a microscope, the MPFC system has a FoV of 0.16 mm^2 and a lateral resolution of $1.55 \mu\text{m}$, which allow for imaging cells flowing in the microfluidic channel. In addition, the introduction of our designed dual-view transport of intensity phase imaging enables real-time phase reconstruction in high accuracy. The MPFC system has been successfully employed in flowing cell imaging, recognition, and analysis even in high-flowing velocity conditions. Moreover, due to the high frame rates, the MPFC system can also be used for monitoring transient events, such as cell motilities, including rotation and binary rotation. Considering the advantages of the MPFC system as simple configuration, accurate phase retrieval, high imaging contrast, and real-time imaging, this work is expected to promote the application of phase imaging flow cytometry in high-throughput rapid cellular detection and tracking.

Funding. Wuxi Municipal Bureau on Science and Technology (K20221016); Fundamental Research Funds for the Central Universities (JUSRP123028); Natural Science Foundation of Jiangsu Province (BK20200588); National Natural Science Foundation of China (62205126, 62305133).

Disclosures. The authors declare that there are no conflicts of interest related to this article.

Data availability. Data underlying the results presented in this paper are not publicly available at this time but may be obtained from the authors upon reasonable request.

References

1. A. Adan, G. Alizada, and Y. Kiraz, *et al.*, "Flow cytometry: basic principles and applications," *Crit. Rev. Biotechnol.* **37**(2), 163–176 (2017).
2. R.-J. Yang, L.-M. Fu, and H.-H. Hou, "Review and perspectives on microfluidic flow cytometers," *Sens. Actuators, B* **266**, 26–45 (2018).
3. Y. Han, Y. Gu, and A. C. Zhang, *et al.*, "Review: imaging technologies for flow cytometry," *Lab Chip* **16**(24), 4639–4647 (2016).
4. K. Huang, H. Matsumura, and Y. Zhao, *et al.*, "Deep imaging flow cytometry," *Lab Chip* **22**(5), 876–889 (2022).
5. D. M. D. Siu, K. C. M. Lee, and B. M. F. Chung, *et al.*, "Optofluidic imaging meets deep learning: from merging to emerging," *Lab Chip* **23**(5), 1011–1033 (2023).
6. F. Liu, T. Jin, and R. Yan, *et al.*, "An opto-acousto-fluidic microscopic system with a high spatiotemporal resolution for microfluidic applications," *Opt. Express* **27**(2), 1425–1432 (2019).
7. T. Jin, C. Zhang, and F. Liu, *et al.*, "On-chip multicolor photoacoustic imaging flow cytometry," *Anal. Chem.* **93**(23), 8134–8142 (2021).
8. A. Sun, T. Li, and T. Jin, *et al.*, "Acoustic standing wave aided multiparametric photoacoustic imaging flow cytometry," *Anal. Chem.* **93**(44), 14820–14827 (2021).
9. Y. Han and Y. H. Lo, "Imaging cells in flow cytometer using spatial-temporal transformation," *Sci. Rep.* **5**(1), 13267 (2015).
10. A. Mahjoubfar, C. Chen, and K. R. Niazi, *et al.*, "Label-free high-throughput cell screening in flow," *Biomed. Opt. Express* **4**(9), 1618–1625 (2013).
11. Q. T. Lai, K. C. Lee, and A. H. Tang, *et al.*, "High-throughput time-stretch imaging flow cytometry for multi-class classification of phytoplankton," *Opt. Express* **24**(25), 28170–28184 (2016).

12. A. K. Lau, H. C. Shum, and K. K. Wong, *et al.*, "Optofluidic time-stretch imaging - an emerging tool for high-throughput imaging flow cytometry," *Lab Chip* **16**(10), 1743–1756 (2016).
13. E. D. Diebold, B. W. Buckley, and D. R. Gossett, *et al.*, "Digitally synthesized beat frequency multiplexing for sub-millisecond fluorescence microscopy," *Nat. Photonics* **7**(10), 806–810 (2013).
14. D. Schraivogel, T. M. Kuhn, and B. Rauscher, *et al.*, "High-speed fluorescence image-enabled cell sorting," *Science* **375**(6578), 315–320 (2022).
15. W. Yan, J. Wu, and K. K. Y. Wong, *et al.*, "A high-throughput all-optical laser-scanning imaging flow cytometer with biomolecular specificity and subcellular resolution," *J. Biophotonics* **11**(2), e201700178 (2018).
16. J. Wu, A. H. L. Tang, and A. T. Y. Mok, *et al.*, "Multi-MHz laser-scanning single-cell fluorescence microscopy by spatiotemporally encoded virtual source array," *Biomed. Opt. Express* **8**(9), 4160–4171 (2017).
17. E. Schonbrun, P. E. Steinvurzel, and K. B. Crozier, "A microfluidic fluorescence measurement system using an astigmatic diffractive microlens array," *Opt. Express* **19**(2), 1385–1394 (2011).
18. A. Ahmad, F. Sala, and P. Paie, *et al.*, "On the robustness of machine learning algorithms toward microfluidic distortions for cell classification via on-chip fluorescence microscopy," *Lab Chip* **22**(18), 3453–3463 (2022).
19. E. Schonbrun, G. Di Caprio, and D. Schaak, "Dye exclusion microfluidic microscopy," *Opt. Express* **21**(7), 8793–8798 (2013).
20. E. Schonbrun, R. Malka, and G. Di Caprio, *et al.*, "Quantitative absorption cytometry for measuring red blood cell hemoglobin mass and volume," *Cytometry* **85**(4), 332–338 (2014).
21. G. Di Caprio, C. Stokes, and J. M. Higgins, *et al.*, "Single-cell measurement of red blood cell oxygen affinity," *Proc. Natl. Acad. Sci. U. S. A.* **112**(32), 9984–9989 (2015).
22. H. Yamada, A. Hirotsu, and D. Yamashita, *et al.*, "Label-free imaging flow cytometer for analyzing large cell populations by line-field quantitative phase microscopy with digital refocusing," *Biomed. Opt. Express* **11**(4), 2213–2223 (2020).
23. N. A. Turko and N. T. Shaked, "Erythrocyte volumetric measurements in imaging flow cytometry using simultaneous three-wavelength digital holographic microscopy," *Biomed. Opt. Express* **11**(11), 6649–6658 (2020).
24. D. Pirone, M. Mugnano, and P. Memmolo, *et al.*, "Three-dimensional quantitative intracellular visualization of graphene oxide nanoparticles by tomographic flow cytometry," *Nano Lett.* **21**(14), 5958–5966 (2021).
25. M. Mir, H. Ding, and Z. Wang, *et al.*, "Blood screening using diffraction phase cytometry," *J. Biomed. Opt.* **15**(2), 027016 (2010).
26. C. Song, Z. Chen, and X. Zheng, *et al.*, "Growth characteristic analysis of haematococcus pluvialis in a microfluidic chip using digital in-line holographic flow cytometry," *Anal. Chem.* **94**(15), 5769–5775 (2022).
27. A. Sun, X. He, and Z. Jiang, *et al.*, "Phase flow cytometry with coherent modulation imaging," *J. Biophotonics* **16**(7), e202300057 (2023).
28. L. Waller, S. S. Kou, and C. J. Sheppard, *et al.*, "Phase from chromatic aberrations," *Opt. Express* **18**(22), 22817–22825 (2010).
29. C. Zuo, Q. Chen, and W. Qu, *et al.*, "Noninterferometric single-shot quantitative phase microscopy," *Opt. Lett.* **38**(18), 3538–3541 (2013).
30. Y. Li, J. Di, and C. Ma, *et al.*, "Quantitative phase microscopy for cellular dynamics based on transport of intensity equation," *Opt. Express* **26**(1), 586–593 (2018).
31. P. M. Blanchard, D. J. Fisher, and S. C. Woods, *et al.*, "Phase-diversity wave-front sensing with a distorted diffraction grating," *Appl. Opt.* **39**(35), 6649–6655 (2000).
32. W. Yu, X. Tian, and X. He, *et al.*, "Real time quantitative phase microscopy based on single-shot transport of intensity equation (ssTIE) method," *Appl. Phys. Lett.* **109**(7), 071112 (2016).
33. L. Waller, Y. Luo, and S. Y. Yang, *et al.*, "Transport of intensity phase imaging in a volume holographic microscope," *Opt. Lett.* **35**(17), 2961–2963 (2010).
34. X. Tian, W. Yu, and X. Meng, *et al.*, "Real-time quantitative phase imaging based on transport of intensity equation with dual simultaneously recorded field of view," *Opt. Lett.* **41**(7), 1427–1430 (2016).
35. Y. Shan, Q. Gong, and J. Wang, *et al.*, "Measurements on ATP induced cellular fluctuations using real-time dual view transport of intensity phase microscopy," *Biomed. Opt. Express* **10**(5), 2337–2354 (2019).
36. C. Chen, Y. N. Lu, and H. Huang, *et al.*, "PhaseRMiC: phase real-time microscope camera for live cell imaging," *Biomed. Opt. Express* **12**(8), 5261–5271 (2021).
37. X. Xing, L. Zhu, and C. Chen, *et al.*, "Transformer oil quality evaluation using quantitative phase microscopy," *Appl. Opt.* **61**(2), 422–428 (2022).
38. C. Chen, Y. Gu, and Z. Xiao, *et al.*, "Automatic whole blood cell analysis from blood smear using label-free multi-modal imaging with deep neural networks," *Anal. Chim. Acta* **1229**, 340401 (2022).